Research Article | Vol. 26, No. 19 | 17 Sep 2018 | OPTICS EXPRESS 24372
Optics EXPRESS

Multifunctional waveguide interferometer sensor: simultaneous detection of refraction and absorption with size-exclusion function

CHEN ZHOU, MEHDI KESHAVARZ HEDAYATI, AND ANDERS KRISTENSEN*

Department of Micro- and Nanotechnology, Technical University of Denmark, DK-2800 Kongens Lyngby, Denmark
anders.kristensen@nanotech.dtu.dk

Abstract: A waveguide Young interferometer is presented with simultaneous detection of complex refractive index of a liquid sample. The real part of the refractive index change (refraction) is detected by tracing phase shifts of the interferogram generated by a sensing and reference waveguide. The imaginary part of the refractive index (absorption) is determined by the attenuation of the transmitted signal at certain wavelength. Furthermore, nano-filters are fabricated atop the sensing waveguide, which enables size-exclusion filtering of species to the evanescent field. It shows capability of distinguishing small and large particles from 100 nm to 500 nm in diameter, which is further confirmed by fluorescent excitation experiments. The present sensor could find broad application in optical characterization of complex turbid media with regard to their complex refractive index.

OCIS codes: (130.5460) Polymer waveguides; (120.3180) Interferometry; (280.4788) Optical sensing and sensors.

References and links

1. P. Kozma, F. Kehl, E. Ehrentreich-Förster, C. Stamm, and F. F. Bier, "Integrated planar optical waveguide interferometer biosensors: A comparative review," Biosens. Bioelectron. **58**, 287–307 (2014).
2. K. Schmitt, K. Oehse, G. Sulz, and C. Hoffmann, "Evanescent field sensors based on tantalum pentoxide waveguides - A review," Sensors. **8**, 711–738 (2008).
3. V. J. Cadarso, A. Llobera, M. Puyol, and H. Schift, "Integrated photonic nanofences: Combining subwavelength waveguides with an enhanced evanescent field for sensing applications," ACS Nano **10**, 778–785 (2016).
4. S. C. A. H. Olmstrom, T. O. D. D. H. S. Tievater, D. M. A. K. Ozak, M. A. W. P. Ruessner, N. A. T. Yndall, W. I. S. R. Abinovich, R. A. N. M. C. G. Ill, and J. A. B. K. Hurgin, "Trace gas Raman spectroscopy using functionalized waveguides," Optica **3,** 891 (2016).
5. P. Polynkin, A. Polynkin, N. Peyghambarian, and M. Mansuripur, "Evanescent field-based optical fiber sensing device for measuring the refractive index of liquids in microfluidic channels," Opt. Lett. **30**, 1273 (2005).
6. C. F. Carlborg, K. B. Gylfason, A. Kaźmierczak, F. Dortu, M. J. Bañuls Polo, A. Maquieira Catala, G. M. Kresbach, H. Sohlström, T. Moh, L. Vivien, J. Popplewell, G. Ronan, C. A. Barrios, G. Stemme, and W. Van Der Wijngaart, "A packaged optical slot-waveguide ring resonator sensor array for multiplex label-free assays in labs-on-chips," Lab Chip **10**, 281–290 (2010).
7. L. Stern, A. Naiman, G. Keinan, N. Mazurski, M. Grajower, and U. Levy, "Ultra-precise optical to radio frequency based chip-scale refractive index and temperature sensor," Optica **4**, 1 (2017).
8. S. Aikio, J. Hiltunen, J. Hiitola-Keinänen, M. Hiltunen, V. Kontturi, S. Siitonen, J. Puustinen, and P. Karioja, "Disposable photonic integrated circuits for evanescent wave sensors by ultra-high volume roll-to-roll method," Opt. Express **24**, 2527 (2016).
9. M. Hofmann, Y. Xiao, S. Sherman, U. Gleissner, T. Schmidt, and H. Zappe, "Asymmetric Mach-Zehnder inter-ferometers without an interaction window in polymer foils for refractive index sensing," Appl. Opt. **55**, 1124 (2016).
10. V. J. Cadarso, N. Chidambaram, L. Jacot-Descombes, and H. Schift, "High-aspect-ratio nanoimprint process chains," Microsyst. Nanoeng. **3**, 17017 (2017).
11. C. Y. Chao and L. J. Guo, "Biochemical sensors based on polymer microrings with sharp asymmetrical resonance," Appl. Phys. Lett. **83**, 1527–1529 (2003).
12. A. Ksendzov and Y. Lin, "Integrated optics ring-resonator sensors for protein detection," Opt. Lett. **30**, 3344 (2005).
13. C. Y. Chao, W. Fung, and L. J. Guo, "Polymer microring resonators for biochemical sensing applications," IEEE J. Sel. Top. Quantum Electron. **12**, 134–142 (2006).

#337953 https://doi.org/10.1364/OE.26.024372
Journal © 2018 Received 6 Jul 2018; revised 23 Aug 2018; accepted 28 Aug 2018; published 4 Sep 2018

Optics EXPRESS

14. Y. Xiao, S. A. Mendez, M. Hofmann, M. Gauch, H. Ehlers, D. Ristau, C. Mueller, and H. Zappe, "Sensitivity enhancement of polymeric Mach-Zehnder interferometers by use of thin high-index films," Sens. Actuat. A: Phys. **265**, 181–186 (2017).
15. M. Hiltunen, J. Hiltunen, P. Stenberg, J. Petäjä, E. Heinonen, P. Vahimaa, and P. Karioja, "Polymeric slot waveguide at visible wavelength," Opt. Lett. **37**, 4449 (2012).
16. N. Nilius, T. M. Wallis, and W. Ho, "Influence of a Heterogeneous Al 2 O 3 Surface on the Electronic Properties of Single Pd Atoms," Opt. Express **25**, 2–5 (2003).
17. L. Ahmadi, M. Hiltunen, P. Stenberg, J. Hiltunen, S. Aikio, M. Roussey, J. Saarinen, and S. Honkanen, "Hybrid layered polymer slot waveguide Young interferometer," Opt. Express **24**, 10275 (2016).
18. M. Hiltunen, J. Hiltunen, P. Stenberg, S. Aikio, L. Kurki, P. Vahimaa, and P. Karioja, "Polymeric slot waveguide interferometer for sensor applications," Opt. Express **22**, 7229 (2014).
19. M. Wang, J. Hiltunen, C. Liedert, S. Pearce, M. Charlton, L. Hakalahti, P. Karioja, and R. Myllylä, "Highly sensitive biosensor based on UV-imprinted layered polymeric-inorganic composite waveguides," Opt. Express **20**, 20309 (2012).
20. P. G. Hermannsson, K. T. Sørensen, C. Vannahme, C. L. Smith, J. J. Klein, M.-M. Russew, G. Grützner, and A. Kristensen, "All-polymer photonic crystal slab sensor," Opt. Express **23**, 16529 (2015).
21. M. Häyrinen, M. Roussey, A. Säynätjoki, M. Kuittinen, and S. Honkanen, "Titanium dioxide slot waveguides for visible wavelengths." Appl. optics **54**, 2653–7 (2015).
22. C. Zhou, M. Keshavarz Hedayati, X. Zhu, F. Nielsen, U. Levy, and A. Kristensen, "Optofluidic Sensor for Inline Hemolysis Detection on Whole Blood," ACS Sensors **3**, 784–791 (2018).
23. B. T. Cunningham, P. Li, S. Schulz, B. Lin, C. Baird, J. Gerstenmaier, C. Genick, F. Wang, E. Fine, and L. Laing, "Label-free assays on the BIND system," J. Biomol. Screen. **9**, 481–490 (2004).
24. K. Schmitt, B. Schirmer, C. Hoffmann, A. Brandenburg, and P. Meyrueis, "Interferometric biosensor based on planar optical waveguide sensor chips for label-free detection of surface bound bioreactions," Biosens. Bioelectron. **22**, 2591–2597 (2007).
25. D. R. Lide, *CRC Handbook of Chemistry and Physics*, eBook. p. 3485 (2003).
26. K. Sørensen, C. Ingvorsen, L. Nielsen, and A. Kristensen, "Effects of water-absorption and thermal drift on a polymeric photonic crystal slab sensor," Opt. Express **26**, 5416–5422 (2018).
27. C. Stamm, R. Dangel, and W. Lukosz, "Biosensing with the integrated-optical difference interferometer: dual-wavelength operation," Opt. Commun. **153**, 347–359 (1998).
28. G. R. J. T. Riggs, Y. U. E. W. Ang, C. H. P. R. Eardon, M. A. F. Ischer, G. A. J. O. E. Vans, and T. H. F. K. Rauss, "Chirped guided-mode resonance biosensor," Optica. **4**, 1–6 (2017).
29. W. Lukosz, C. Stamm, H. Moser, R. Ryf, and J. Dübendorfer, "Difference interferometer with new phase-measurement method as integrated-optical refractometer, humidity sensor and biosensor," Sens. Actuat. B: Chem. **39**, 316–323 (1997).
30. A. Brandenburg, "Differential refractometry by an integrated-optical Young interferometer," Sens. Actuat. B: Chem. **39**, 266–271 (1997).
31. M. Wang, S. Uusitalo, C. Liedert, J. Hiltunen, L. Hakalahti, and R. Myllylä, "Polymeric dual-slab waveguide interferometer for biochemical sensing applications," Appl. Opt. **51**, 1886 (2012).
32. D. J. Rowe, D. Smith, and J. S. Wilkinson, "Complex refractive index spectra of whole blood and aqueous solutions of anticoagulants, analgesics and buffers in the mid-infrared," Sci. Rep. **7**, 1–9 (2017).
33. A. Bavali, P. Parvin, S. Z. Mortazavi, M. Mohammadian, and M. R. Mousavi Pour, "Red/blue spectral shifts of laser-induced fluorescence emission due to different nanoparticle suspensions in various dye solutions," Appl. Opt. **53**, 5398 (2014).
34. W. M. b. M. Yunus, "Refractive index of dye solution," Appl. Opt. **28**, 4268 (1989).
35. B. Jaskorzynska, Y. Song, and M. Qiu, "Tradeoff between mode confinement, loss, and cross-talk, for dielectric and metal slot waveguides," Photonics Lett. Pol. **1**, 172–174 (2009).
36. S. M. Yoo and S. Y. Lee, "Optical Biosensors for the Detection of Pathogenic Microorganisms," Trends Biotechnol. **34**, 7–25 (2016).
37. G. Luka, A. Ahmadi, H. Najjaran, E. Alocilja, M. Derosa, K. Wolthers, A. Malki, H. Aziz, A. Althani, and M. Hoorfar, "Microfluidics integrated biosensors: A leading technology towards lab-on-A-chip and sensing applications," Sensors (Switzerland) **15**, 30011–30031 (2015).

1. Introduction

Optical waveguides have been widely used as efficient sensors for detection of refractive index (RI) change by probing near the surface region of the sample with the evanescent field [1–7]. Recently, polymer waveguides have gained much attention owing to their interesting properties including high transparency in the UV-visible range, versatile process-abilities, cost effectiveness, and mechanical flexibility [8–10]. Different designs including ring resonators [11–13], interferometers [14–19] and guided mode resonance filters [20] have been demonstrated. In order to enhance the

Optics EXPRESS

sensitivity of the polymeric sensor, various strategies have been demonstrated. Organic-inorganic polymer slot waveguides have been developed to enable large light-liquid interaction [15, 17, 21]. Some polymer waveguides have shown enhanced sensitivity by incorporating additional high RI material like TiO_2 and Ta_2O_5 at the interface to the liquid, [2, 14, 16, 17]. However, simultaneous measurement of both the real and imaginary component of refractive index has been less explored. Here, we address this issue and present a sensor that is able to detect real and imaginary part of the refractive index at the same time using a Young interferometer. Furthermore, we added size-exclusion sensing functionalities, which has been demonstrated in our previous work for detection of hemolysis in whole blood [22]. The multi-functionality can significantly expand the applicability of the sensor in to areas dealing with complex turbid medium.

The interferometer sensor presented in this work (Fig. 1) comprises two waveguides (sensing and reference) with individual grating couplers for both in- and out-coupling. The sensing waveguide has nano-filters atop with an opening of 200 nm that enable local exclusion to the evanescent field, enabling size dependent detection. With help of the grating couplers, the finished sensors are highly integrated and can be individually addressed and applied without need of dicing [8, 15, 17, 19]. This feature enables a compact parallelization of the sensor, which is applicable in various sensing platforms such as embedding to the bottom of a microtiter plate [23]. We measured ethanol water mixture to calibrate the bulk RI sensitivity as well as a dye solution for absorption measurement. Here, both the phase shift due to the real part of RI (n) and the absorption due to the imaginary part (k) can be obtained. The size-exclusion function was verified by measuring solutions containing polystyrene nanoparticles of different sizes. Moreover, we use the waveguide evanescent field for fluorescent excitation to excite fluorescent nanoparticles with different sizes, which further proves the size-selectivity of the waveguide sensor.

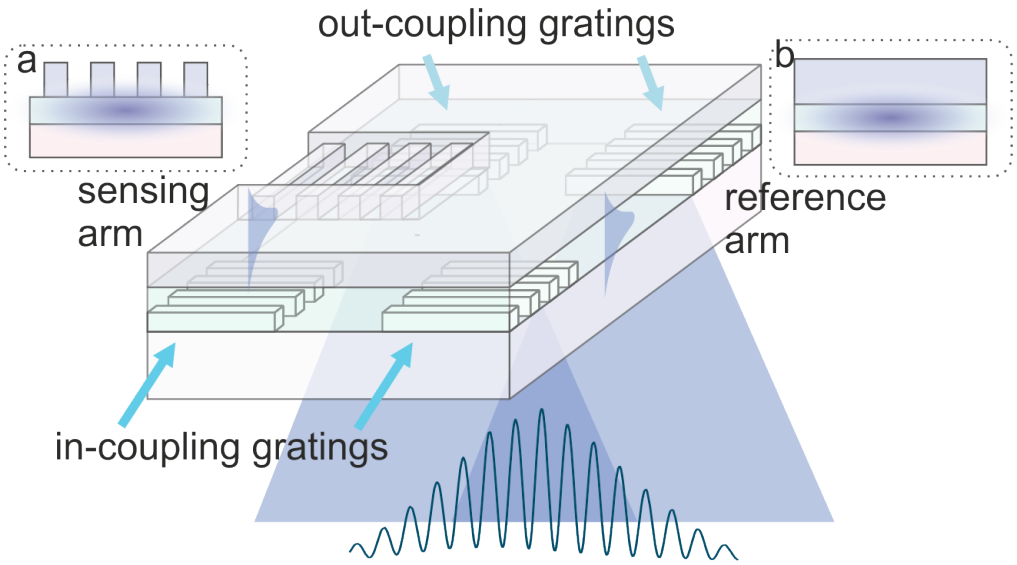

Fig. 1. Illustration of the waveguide interferometer. A sensing and a reference waveguide is placed beside each other. A sensing window with nano-filters is exposed to the liquid, where the rest of the sensor is passivated by a thick layer of polymer. The light is coupled by the in-coupling gratings into the waveguides, while the guided light is out-coupled by the out-coupling gratings and generates an interference pattern on the line camera. Insets (a-b) in dashed windows show the cross section of the sensing and reference arm.

Optics EXPRESS

2. Design and fabrication of the interferometer with size-exclusion filters

2.1. Design of a grating-coupled Young interferometer

The schematic image in Fig. 1 illustrates the design of the device. We aimed to generate a Young interferometer with two slab waveguides with grating couplers for in- and out-coupling. Instead of using a Y-splitter to generate two waveguides from one [18, 19], we used two grating couplers to define two slab waveguides. The latter avoids lateral confinement of the guided light in the slab waveguide and simplifies the fabrication process. A gap of 200 μm between the grating couplers defines the distance between the fringes of the interferogram. The total propagation length of the waveguide on the chip is 3.4 mm. The active sensing length is given by the area where the waveguide is exposed to the liquid, as shown in the sensing arm of the Fig. 1. This length is 800 μm in our design, where a larger length can further amplify the total phase shift, as will be discussed later. For the light source, a laser module with 450 nm wavelength (CPS450, Thorlabs) is used. The laser produces a continuous beam with an output power of 4.5 mW, which is sufficient for this application. The laser beam is linearly polarized and focused with a single convex lens (focal length 100 mm). The large focal length gives a low numerical aperture which is preferred for coupling into an equidistant grating coupler for its narrow acceptance angle. The beam size is chosen large enough to be able to couple into the two grating couplers (for sensing and reference arms) at the same time, which eliminates the need of an additional beam splitter. The out-coupled light can scatter laterally to generate an interferogram to be captured by a line camera as shown in Fig. 2(a). The Fourier transformed signal is shown in Fig. 2(b), where a sharp frequency appears, shows the efficiency of the grating coupled Young-interferometer even without any additional slits as used in other works [24].

2.2. Design of the waveguide with nano-filters

The sensitivity of the interferometer sensor depends on by the mode overlap between the guided light and the liquid sample. Slot waveguides are widely used for their large mode overlap as the guided mode can reside in the low refractive index medium [17]. For the sensing arm, we aim to achieve high sensitivity while maintaining the functionality as local filters. UV-nanoimprinted OrmoComp (micro resist technology GmbH, Germany) ridges atop the waveguide core function as filters, as shown in Fig. 2(c). Here, we did waveguide mode analysis with COMSOL Multiphysics (COMSOL Inc., Sweden). For the simulation, we used the real dimensions of the fabricated device. The RI values of the materials are measured with an ellipsometer and used in the simulation. A wavelength of 450 nm is used for the simulation, which is also the operation wavelength of the interferometer. At 450 nm wavelength, the following RI values are given: 1.53 (nano-filter, OrmoComp), 1.62 (waveguide core, OrmoClear), and 1.41 (cladding, Efiron). The periodicity of the filters is 400 nm, where two filters are simulated as a unit cell. Thus, a periodic boundary condition of 800 nm is created. The width of the filters is 180 nm and the height is 250 nm. These values are obtained by SEM inspection.

The simulation result of the transverse electric (TE) mode, which is horizontally aligned, is shown in Fig. 2(c). It is clear that the mode is strongly confined under the top of the nano-filters. The strongest mode intensity is inside the waveguide core. In the middle of a nano-well, the energy density of the fundamental TE mode is only 2.3% at the top (250 nm high) compared to the bottom. Since the evanescent field is confined under the ridges, large species in the bulk liquid are not interacting with the guided light, enabling size exclusive detection. To enable the confinement for the device, we chose a high RI polymer (OrmoClear H101, micro resist technology GmbH, Germany) as the waveguide core. The material is doped with ZrO_2 to achieve high RI (1.62 at 450 nm) while being highly transparent in the visible range [20]. The material for the nano-filters (OrmoComp) and the cladding (Efiron, Luvantix, South Korea) exhibit a RI of 1.53 and 1.41 at 450 nm, respectively. The contrast from OrmoComp cover material to the

Optics EXPRESS

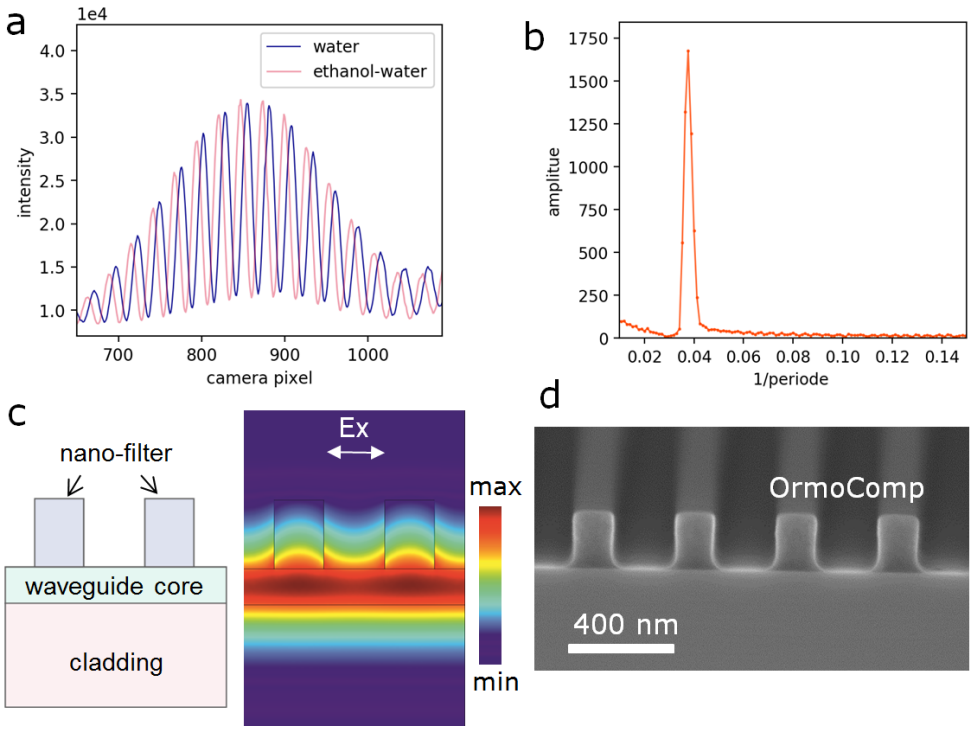

Fig. 2. a) The interferograms captured by the line camera of water and an ethanol-water solution. b) The amplitude of the Fourier transformed interferogram. c) Illustration and the optical simulation of the TE mode of the waveguide. The mode is confined underneath the top of the filters to avoid interference from the bulk. d) SEM image of imprinted nano-filters (OrmoComp) on a Si substrate. Little imprint residue can be seen.

waveguide core as well as cladding has to be chosen carefully as the grating coupler areas are made of the same materials. A low contrast in RI can also lead to lower coupling efficiency, as the gratings are covered in OrmoComp material, as shown in Fig. 1. The thickness of the waveguide core is chosen to be low (140 nm) in order to enable the maximum evanescent mode overlap with liquid. The effective refractive index of the waveguide with nano-filters is 1.485 (TE mode, horizontally polarized, water used as buffer n = 1.338), while the reference waveguide has a n_{eff} = 1.533.

2.3. Fabrication

The fabrication process is adapted from our previous work [22]. A process flow is illustrated in Fig. 3. A brief description is as follows: 1) we drop-cast the Efiron polymer onto a glass substrate and the grating couplers are formed in the surface by UV nanoimprint lithography. The Si stamp is made by E-beam lithography with etched gratings (390 nm in pitch). 2) Core material OrmoClear HI01 is spin-coated onto the surface of the cladding material. By adjusting the dilution and spin-coating velocity, the core thickness is controlled. 3) A thin layer OrmoComp (140 nm) is spin-coated to the cured OrmoClear surface, followed by a UV-nanoimprint step to define the nano-filters. 4) A thick layer of OrmoComp layer (8 μm) is spin-coated, followed by a photolithography step for opening the sensing windows, leaving the reference waveguide isolated. The challenge is to obtain a residue free imprint of the nano-filter(cf. Fig. 2(d)), since a residual layer will decrease the sensitivity of the waveguide. We use a stamp made of

Optics EXPRESS

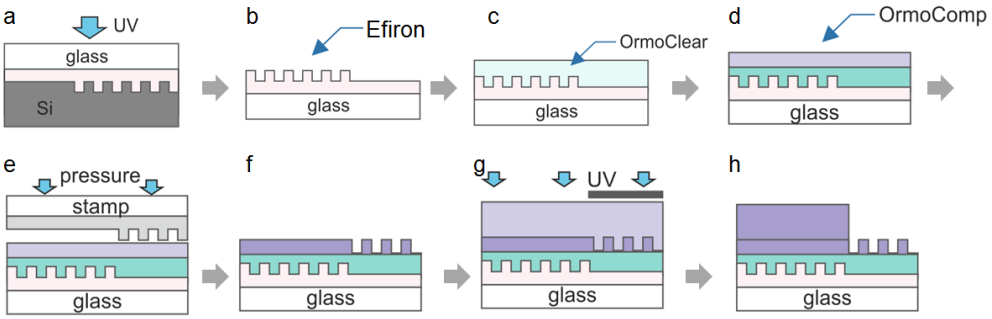

Fig. 3. Fabrication process of the hybrid polymer interferometer device. a) Efiron polymer is imprinted on a glass substrate with a Si master stamp to define grating couplers. b) The Si master stamp is removed. c) OrmoClear is spin-coated onto Efiron cladding and cured with UV exposure. d) A thin layer of OrmoComp is spin-coated. e) A transparent stamp made of OrmoStamp on glass substrate is used to imprint the OrmoComp layer. f) The OrmoComp layer is UV-cured and nano-filters are defined. g) A thick layer of OrmoComp is spin-coated and UV lithography is carried out. h) The filter region is opened after removal of the uncured polymer.

OrmoStamp (micro resist technology, Germany) to enable a homogeneous imprint with low stamp bending and low residual layer. The OrmoStamp stamp is a replica of the E-beam written Si stamp and grafted with perfluorodecyltrichlorosilane (FDTS) for anti-sticking surface. A molecular vapor deposition process was used by subsequently applying O_2 plasma and FDTS (MVD 100, Applied Microstructures Inc. , USA). A demonstration of the nano-filter imprint is shown in Fig. 2(d), where it is made on Si wafer for better SEM imaging. The pitch of the filters is 400 nm and the width is 180 nm, which leaves an opening of 220 nm for the liquid interaction.

3. Performance of the interferometer sensor

3.1. Measurement of ethanol-water mixture

To verify the sensitivity of the sensor we performed a series of measurements with ethanol-water mixture. A laser at 450 nm was used, while a CMOS line camera (S11639-01, Hamamatsu, Japan) captures the signal in a one second interval for time-resolved measurement. A PMMA housing is taped onto the sensor to define the fluidic path on the interferometer. We mixed ethanol-water solutions of various concentrations (0.1 %, 0.2%, 0.5%, 0.75%, 1% by weight). The RI change of the medium Δn_c of different ethanol-water is calculated as $\Delta n_c = 6.6 \cdot 10^{-4} \cdot C_{eth}$ where C_{eth} is the percentage by weight of ethanol in water. Here, we have adapted the empirical value to our working wavelength at 450 nm [25]. Prior to the experiments with ethanol-water solution, we prepared the sensor by filling the channel with DI water for at least 4 hours to saturate the water absorption of the polymer [19, 26].

The phase change is calculated by monitoring the spatial displacement of the interference fringes. The frequency domain of the original spatial signal is calculated by a fast Fourier transform (FFT) algorithm. The peak of the amplitude in the frequency domain corresponds to the fringes that are generated by the waveguide interference, as shown in Fig. 2(b). With the knowledge of the relevant frequency, the argument at that frequency can be used to calculate the time-dependent phase shifts. In Fig. 4(a)-4(b), the phase shifts of the 1 and 0.1 wt.% ethanol-water solution are plotted. The first two minutes, the sensor is exposed to DI water followed by exposure to ethanol-water mixture (with gray background). Then, the sensor is rinsed with DI water again.

Optics EXPRESS

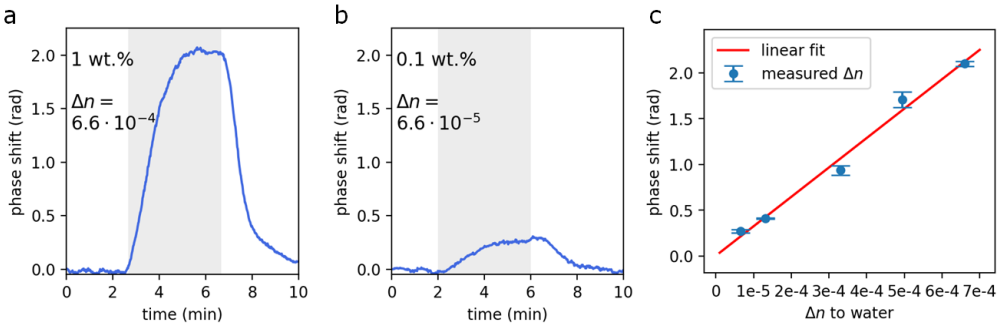

Fig. 4. a) and b) Time-resolved phase shifts recorded for applying ethanol-water solution with different weight concentration to water. The gray areas indicate the influx of ethanol-water solution. c) Plot of measured the phase shifts from different ethanol-water solution. The RI change is calculated and plotted on the x axis. The linear fit shows the linearity of the phase shift to the bulk RI change.

For all concentrations, three measurements are made, of which the standard deviation is plotted as error bar in Fig. 4(b). The smallest concentration we measured is 0.1 wt.% ethanol in water ($\Delta n = 6.6 \times 10^{-5}$). The three repeated measurements showed a standard deviation in phase shift of 0.0175 rad, which can be calculated to a limit of detection of 1.7×10^{-5} RI unit with LoD = 3σ. Note that the sensor has an effective length of 0.8 mm, which limits the phase shift since the phase shift is given as follows [27]:

$$\Delta\phi = 2\pi L \frac{\Delta\widetilde{n}_{eff}}{\lambda} = 2\pi L \frac{\Delta n_{eff,sen} - \Delta n_{eff,ref}}{\lambda}, \tag{1}$$

where $\Delta\phi$ denotes the phase shift to be measured, L the length of the sensing waveguide (exposed to the liquid), λ the operation wavelength, $\widetilde{n}_{eff}$ the total difference in the effective RI, which is defined as the difference between the RI of the sensing arm $\Delta n_{eff,sen}$ and $\Delta n_{eff,ref}$. In order to achieve a lower detection limit, a strategy is to increase the length of the sensor. The largest length, i.e. phase shift per RI unit, that can be used is only limited to the loss of the sensor. By using a short wavelength laser (450 nm), a large increase in phase shift is realized in comparison to most of previous works [9, 14, 15, 18, 21, 26, 28–30], which operates with a laser above 630 nm. The sensitivity for homogeneous bulk RI sensing of this sensor is comparable to those made by only polymers [9, 19, 31] or optical fiber [5]. We remark that approaches like coating with high RI dielectrics can be employed to enhance the LoD [14, 17]. However, it may compromise the size-exclusion functionality of the sensor. The dynamic range of the refractive index sensing by the waveguide sensor is determined by the cut-off wavelength of the waveguide. In our case, a refractive index between 1.0 and 1.52 can be measured which is determined by the refractive index of the filter material used (1.53, OrmoComp).

3.2. *Measurement of both real and imaginary part of the refractive index*

Since we can adjust the relative intensity of the sensing and reference waveguide, an interferogram with both intensity and phase shift information can be easily generated, as shown in Fig. 5(a). In this case the intensity of the light to be transmitted through the sensing waveguide (relative to the reference waveguide) is increased in order to obtain more intensity information. As we can see from Fig. 5(a), the high frequency waveform has an envelope of a base signal, where the latter is used to evaluate the transmitted intensity. We prepared a dye solution with 100-600 mg/dL tartrazine in water. Tartrazine has an absorption maximum around 435 nm, while the laser is operating at 450 nm. In Fig. 5(a), both intensity attenuation and phase shift are seen. The former

Optics EXPRESS

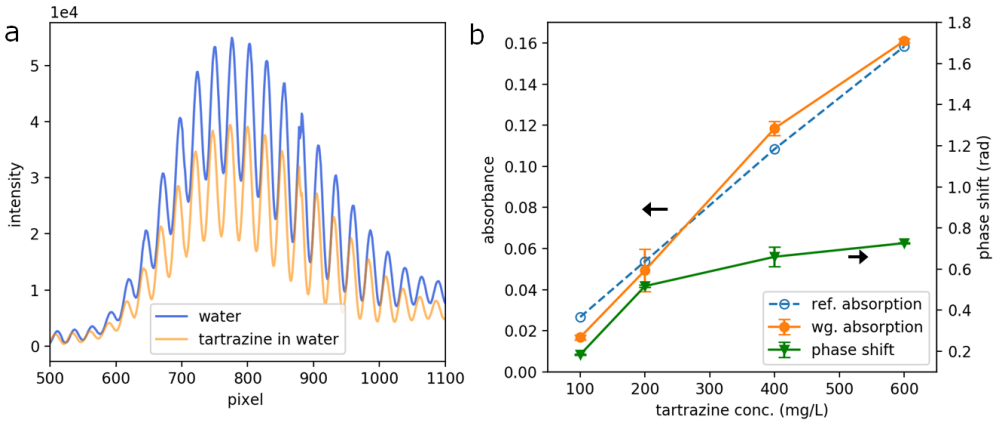

Fig. 5. a) Interferogram of water and a dye solution. The overall intensity is decreased when the sensor is exposed to the tartrazine dye solution. b) Plot of the absorbance (left axis) and phase shift (right axis) measured with the interferometer sensor. Different tartrazine concentrations were mixed into water. The reference absorbance of the dye solutions at the same wavelength (450 nm) is also plotted. The phase shift is evaluated with the same interferogram, which gives the real part of the refractive index.

is caused by the tartrazine absorption - the imaginary part of the refractive index (k), while the latter is caused by the real part of the refractive index (n). However, the original signal involves both phase shift and intensity change and is not ideal for extraction of the attenuation. In order to obtain solely the intensity signal, the interferogram is low-pass filtered by cutting off high frequency signal after the Fourier transformation, as shown in Fig. 6(a)-6(b). The spatial signal that is generated by the interference is thus eliminated, as shown in Fig. 6(c)-6(d). Then, the low-pass filtered signal can be integrated over the whole range to obtain the total transmitted intensity. The absorbance of the solution is then calculated by $a = -\log_{10}(I_{sample}/I_{water})$, where I_{sample} and I_{water} denote the total intensity measured with the sample and rinse, respectively. The absorbance a is linear correlated to the imaginary part, k, of the RI [32]. For the waveguide absorption the relation can be described in the following form:

$$k = \frac{\lambda a}{4\pi\eta d \log_{10} e}, \tag{2}$$

where λ and d are the wavelength and optical path length, respectively, η is the fraction of evanescent energy flux compared to the whole waveguide. Here, we assume zero absorption by the water and use it as the reference signal. In Fig. 5(b) the absorbance is plotted against the reference measurement taken with 1 cm cuvette and a photospectrometer (UV-1800 Shimadzu Corp., Japan). The reference absorbance is linearly scaled to fit the absorbance level of the waveguide. The scale factor f can be used to obtain the evanescent energy factor η by $\eta = f\frac{d_{cuvette}}{d_{waveguide}}$, where $d_{cuvette}$ and $d_{waveguide}$ denote the optical path length of the cuvette and waveguide. The LoD of the absorption measurement is determined to be $3.5 \cdot 10^{-3}$ absorbance, which corresponds to 13 mg/L tartrazine in water. The phase shift of the signal is also plotted to the right axis of Fig. 5(b). In contrast to the absorbance signal, the phase shift is not linear to the concentration of the dye, which is typical for dye solutions [33, 34]. By using the calibration data obtained from the ethanol-water solution, we can determine Δn caused by 600 mg/L tartrazine dye addition to water to be $2.3 \cdot 10^{-4}$.

Optics EXPRESS

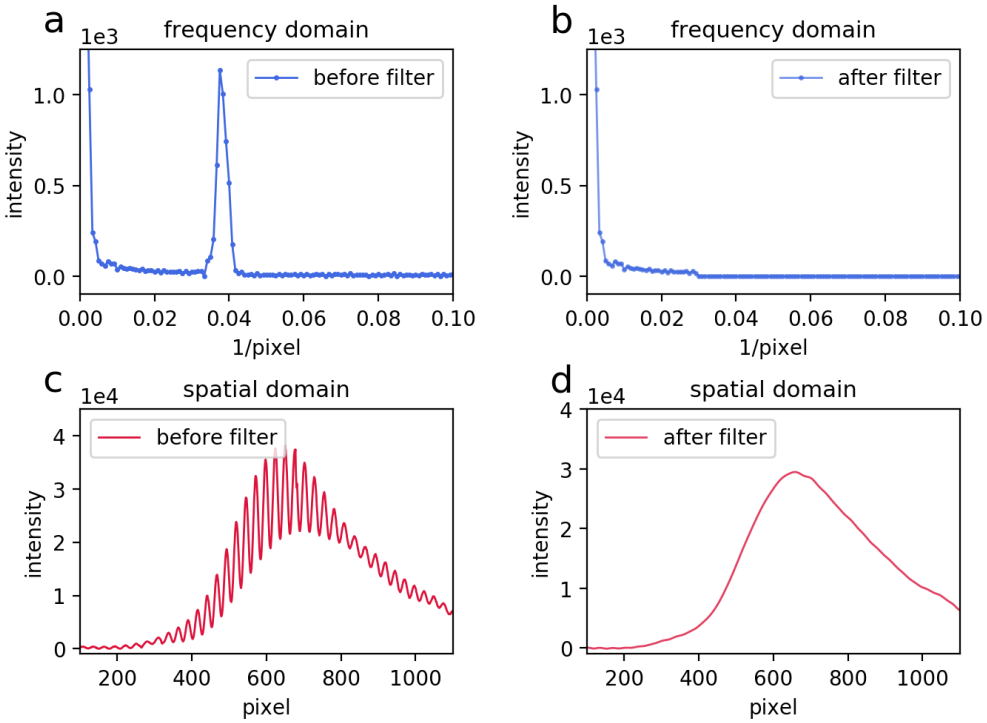

Fig. 6. a) Amplitude of the Fourier-transformed interferogram with a peak which is caused by the waveguide interference. b) Low-pass filtered Fourier-transformed interferogram. The amplitude of the signal that is caused by the interference is set to zero, leaving only bias signal given by the total transmission. c) Interferogram with increased intensity for the sensing waveguide, generating elevated bias signal. d) Inverse Fourier-transformed signal after low-pass filtering. Fringes caused by the interference are eliminated, which can be used to evaluate the attenuation due to absorption.

3.3. *Characterization with nano-beads*

The present waveguide sensor is able to distinguish between small and large objects. We demonstrated the capability by measuring polystyrene nano-beads with different diameters. Two different sizes of 100 and 500 nm (Nanosphere^{TM} Size Standards, Thermo Scientific) were used. A size distribution (standard deviation) of 7.8 and 7.9 nm is given for the 100 and 500 nm nano-beads, respectively. We know that polystyrene has a RI of 1.61 at 450 nm. We diluted the original suspension of the nano-beads from the manufacture to DI water with a volume ratio of 1:1. Then, we centrifuged part of the 500 nm suspension to obtain the pure carrier medium. To measure the phase shift caused by the nano-beads, we use water as rinse and flush 100 nm and 500 nm beads solution as well as the centrifuged medium. The results are shown in Fig. 7. As illustrated, the small beads (100 nm) are able to diffuse into the trenches of 200 nm, while the 500 nm beads are kept outside the evanescent field. Therefore, we observed similar phase shift between the 500 nm beads and the medium. The small change in phase (i.e. the increase in phase shift in the gray area for 500 nm beads) is attributed to the additives given in the original liquid suspension, like surfactants for keeping beads from aggregation. The result demonstrates the ability of the size-exclusion of the sensor. It allows measurement of tiny RI change even with the presence of large particles and impurities, like the 500 nm nano-beads, which renders the liquid completely foggy and intransparent. The threshold of the size-exclusion can be engineered

Optics EXPRESS

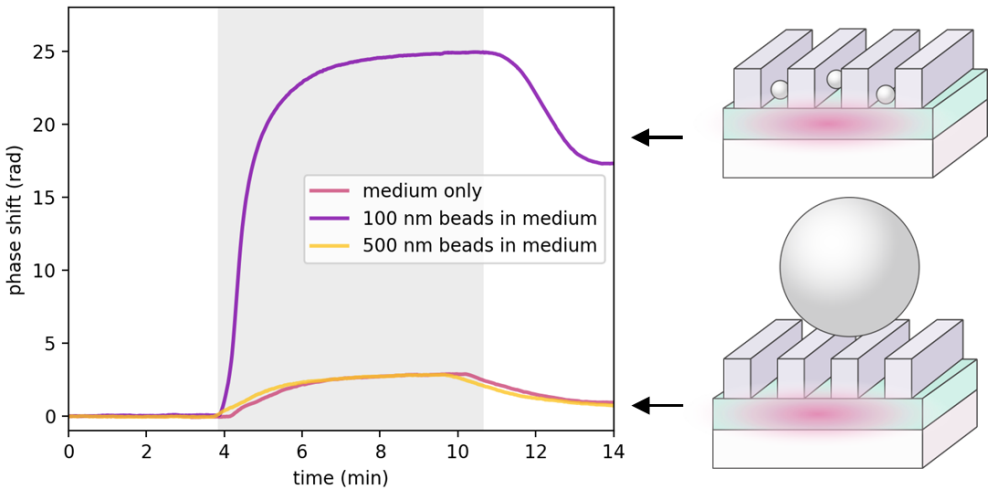

Fig. 7. Time-resolved phase shifts measured with contact to nano-beads suspensions. 100 and 500 nm polystyrene beads were used, where a strong reaction in phase shift is observed with 100 nm beads. The original medium is isolated by centrifugation and measured as well. Little difference is shown between the original medium and the 500 nm beads suspension due to the size exclusion function. The effect of size-exclusion is illustrated schematically on the right side of the graph.

by adjusting the distance of the filers. In comparison to a slot waveguide [15, 17, 21], which also confines the field between high RI ridges, the advantage of our sensor is the flexibility in choosing size threshold as an extra degree of freedom. In our case, the filter and optical (waveguide) designs can be optimized independently. A larger size threshold is easily achieved by increasing the gap size in the filter while the sensitivity can be adjusted correspondingly by changing the waveguide thickness. In contrast, for a slot waveguide, the gap of slots cannot be selected freely [15, 17, 21, 35]. As Fig. 7 shows, the 100 nm solution triggered strong phase shift in the waveguide (see the violet curve). After the rinse, the phase shift does not recover to the original level, which is attributed to the fact that some of the particles are immobilized in between the nano-filters even after the rinse, which cause the raise in the RI to the pure water. Thus, this feature can be utilized to physically immobilize nano-spheres, which can be further utilized as a biosensor [36, 37]. On the other hand, a hydrophilic surface treatment can be used to both waveguide and nano-beads, in order to avoid immobilization of particles, which is beyond the scope of this study.

3.4. *Characterization with fluorescent excitation*

The waveguide can also be utilized for fluorescent excitation with size-exclusion ability. By placing a microscope objective underneath the sensor, the fluorescent signal can be obtained. In our experiment, a 20x microscope objective is used, while a long-pass filter is used before the camera. As demonstrated in Fig. 8(a)-8(b) , both sensing and reference waveguides are excited by the laser light. In Fig. 8(b), the guided light ray is visible due to the auto-fluorescence of the polymers, where in the area of nano-filters there is higher intensity due to scattering. Furthermore, we used three green fluorescent nano-beads with different diameter to visualize the size-excluding excitation (44 nm, 100 nm and 500 nm). For the images in Fig. 8(c)-8(e), the integration time is kept the same (20 ms). It is clear that both 100 nm and 44 nm nano-beads were strongly excited in the filter area. The contrast between

Optics EXPRESS

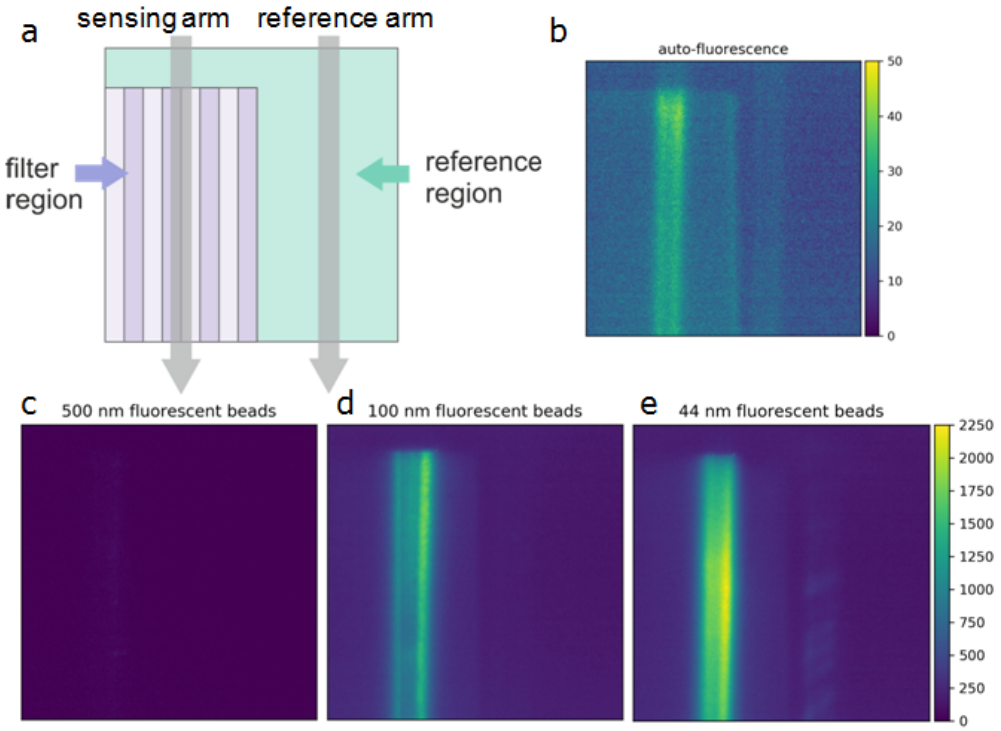

Fig. 8. Fluorescent excitation using waveguide interferometer. a) Illustration of the positions of the sensing and reference waveguide as well as the area of the nano-filters. b) The auto-fluorescence of the waveguide caused by the 450 nm laser excitation. The colorbar used is shown on the right. c-e) Three fluorescent beads (44nm, 100 nm, and 500 nm) are measured with the color bar scaled to the maximum intensity. The integration time remains the same for all measurements.

the intensities of sensing and reference waveguide also proves the viability of the passivation. We remark that we used different sensors for each experiment since the small beads can get stuck in the filter thus contaminates the following measurements. Therefore, small variations in the intensity profile can be observed, which is due to the fact that the coupling condition is slightly different in those experiments. On the other hand, we did not observe significant excitation with the 500 nm beads sample. Only small signal increase can be observed which is mainly due to the scattered light in the liquid. Note that the integration time of the auto-fluorescent experiment is the same as the rest, the maximal intensity is under 50 counts as shown in Fig. 8(b), while the highest intensity achieved by the 100 nm fluorescent beads is at 2250 counts.

4. Conclusion

In this work we demonstrate a highly sensitive waveguide interferometer sensor that is capable of detecting both refraction and absorption which is realized by evaluating the phase shift of the interference fringes and attenuation of the total transmitted signal. In addition, it is paired with size-exclusion functionality to enable optofluidic measurement in complex turbid media. We utilize the confinement of the guided light in the waveguide in which nano-filters atop the waveguide enable exclusion of larger particles in the liquid. A homogeneous bulk RI detection with a LoD in 10^{-5} is shown. Moreover, we used nano-beads to verify the ability of size exclusion

Optics EXPRESS

by means of phase shift and fluorescent excitation. We envision that the sensor can be adopted for various optical detection applications involving small molecules or particles in complex turbid media.

Funding

Innovation Fund Denmark HemoPoc Project (57-2014-3); European Union′s Horizon 2020 Marie Sklodowska-Curie Grant (701597).

Acknowledgment

The authors are grateful to Xiaolong Zhu and Søren Raza for fruitful discussions.